

Model-based and wavelet-based fault detection and diagnosis for biomedical and manufacturing applications:

Leading Towards Better Quality of Life

Imin Kao*, Xiaolin Li and Chia-Hung Dylan Tsai

Department of Mechanical Engineering, SUNY at Stony Brook, Stony Brook, New York 11794-2300, USA

(Received June 5, 2008, Accepted August 24, 2008)

Abstract: In this paper, the analytical fault detection and diagnosis (FDD) is presented using model-based and signal-based methodology with wavelet analysis on signals obtained from sensors and sensor networks. In the model-based FDD, we present the modeling of contact interface found in soft materials, including the biomedical contacts. Fingerprint analysis and signal-based FDD are also presented with an experimental framework consisting of a mechanical pneumatic system typically found in manufacturing automation. This diagnosis system focuses on the signal-based approach which employs multi-resolution wavelet decomposition of various sensor signals such as pressure, flow rate, etc., to determine leak configuration. Pattern recognition technique and analytical vectorized maps are developed to diagnose an unknown leakage based on the established FDD information using the affine mapping. Experimental studies and analysis are presented to illustrate the FDD methodology. Both model-based and wavelet-based FDD applied in contact interface and manufacturing automation have implication towards better quality of life by applying theory and practice to understand how effective diagnosis can be made using intelligent FDD. As an illustration, a model-based contact surface technology can benefit the diabetes with the detection of abnormal contact patterns that may result in ulceration if not detected and treated in time, thus, improving the quality of life of the patients. Ultimately, effective diagnosis using FDD with wavelet analysis, whether it is employed in biomedical applications or manufacturing automation, can have impacts on improving our quality of life.

Keywords: fault detection and diagnosis (FDD), better quality of life, biomedical, manufacturing diagnosis.

1. Introduction

Advances in sensors and sensor technologies in the recent years have paved the way for the growth of research and applications in fault detection and diagnosis (FDD) in various areas such as manufacturing, biomedical applications, modeling of infrastructures and analysis, ..., etc. In this paper, we will present and discuss both (i) model-based FDD, and (ii) signal-based FDD. The model-based FDD will be illustrated with contact modeling as applied in various areas pertaining to daily living. The signal-based FDD using wavelet is applied to prognosis and diagnosis of manufacturing systems which have impacted on our society and quality of life in ways more than one. We present intelligent FDD which will improve the diagnosis and prognosis of systems to enhance the reliability and sustainability.

*Professor, Corresponding author: E-mail: ikao@ms.cc.sunysb.edu

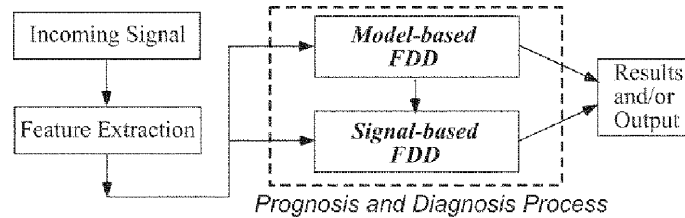


Fig. 1 Flow chart of FDD diagnosis process

Model-based FDD relies on the existence of a physical or mechanical system, which can be employed for the purpose of FDD. For example, a linear model of pneumatic-electrical analogy was used successfully for the detection of leakage, as well as diagnosis of the quantity of leakage in a pneumatic system (Li and Kao 2005). Model-based FDD is typically more applicable to simpler systems with more well-defined physics and system characteristics.

Pattern recognition is an attractive choice for fault diagnosis as this is essentially what an expert or experienced operator does when diagnosing faults. The basic task of pattern recognition is to assign an unknown object or pattern to an appropriate class of a group of similar patterns. The development of a pattern recognition system starts with sensory information using feature extraction, followed by either model-based or signal-based FDD, as illustrated in Fig. 1. Features selection attempts to select or extract important features or attributes in the original data that contain useful information for pattern classification. Feature selection can be aided when appropriate model of the system in consideration exists and can be extracted for comparison. The repeatable feature corresponding to the system model can be utilized for fingerprint analysis and diagnosis. Feature-based approach is suitable for complex systems where waveform signals are used for diagnosis. In such systems, features are considered as random variables. Feature extraction and feature subset selection are critical steps to reduce the number of attributes or data dimension considered in the decision-making process. One procedure to develop a feature-based diagnostic system has been presented in Pittner and Kamarthi (1999), Li and Kao (2004), Li and Kao (2005). In this paper, we specially address the two approaches of FDD, as illustrated in Fig. 1.

Signal processing is also a promising approach for analytical fault detection and diagnosis. Recently, Jin and Shi presented automatic feature extraction of waveform signals for in-process diagnostic performance improvement (Jin and Shi 2001). More application of signal processing techniques in FDD can be found in literature, such as that in Jakubek and Jörgl (2000). In Appendix A, a brief introduction of wavelet transform relevant to this study is presented.

1.1. Research towards better quality of life

The “*better quality of life*” addressed in the paper is somewhat all-encompassing that touches various aspects of our lives. For example, the improvement of health care issues for the aging population or the diabetes through research in contact interface is a way to improve the quality of life. A better FDD tool which can detect faults with proper diagnosis of the faults can improve the efficacy of mechanical and/or pneumatic systems often found in manufacturing automation. Such intelligent FDD systems also improve the quality of our lives directly and indirectly. Other examples of research towards better quality of life are abundant, while we only focus on these two issues in this paper.

1.2. Outline of sections

In this paper, we focus on signal decomposition, diagnosis feature extraction, and intelligent diagnosis. The paper are organized as follows. The model-based FDD is discussed in Section 2 with contact modeling and application of wavelet transform for fingerprint analysis. The signal-based FDD is discussed in Section 3 with wavelet transform for signal decomposition and its application in feature extraction. Next, we discuss an innovative methodology to process and combine features and segment information to form feature vectors and vectorized maps suitable for diagnosis. The conclusion is presented following that.

2. Model-based approach for FDD

Model-based FDD is useful when a physical model of the system in consideration is available. The physical model will dictate the repeatable pattern of fingerprints in the signals which can be used as a basis for FDD. In this section, we present and discuss contact interface and its modeling in general, leading to the discussions of biomedical contact interface such as that in the medical shoes for the diabetics. Since most biomedical tissues and contacts exhibit viscoelastic characteristics, we will introduce and discuss the topic as follows.

2.1. Viscoelastic contact interface and theoretical background

Contact interface is grown out of research in robotics to model both physical and non-direct contacts. In its kinematic rigor, contact imparts constraints across the interface when two bodies are brought into contact; furthermore, the contact interface works like a filter that constrains certain components of forces/moments and motions to transmit through the contact, and render the pressure distribution across the contact patch (Kao, *et al.* 2008).

In order to describe the viscoelastic contact interface, a general approach (Findley, *et al.* 1976) considers the force (N) and the displacement (δ) related by functions in the form of

$$N(t) = G(\delta, t) = N(\delta) \cdot g(t) \quad \text{with } g(0) = 1 \tag{1}$$

$$\delta(t) = H(N, t) = \delta(N) \cdot h(t) \quad \text{with } h(0) = 1 \tag{2}$$

The function G is called the “relaxation function” while the function H is the “creep compliance”. In the general case of nonlinear viscoelasticity, the relaxation function G , as shown in Fig. 2(a), species the force response, as time elapses, to a step displacement from the undeformed configuration; while the creep compliance H , as shown in Fig. 2(b), gives the displacement response to a step force N from the

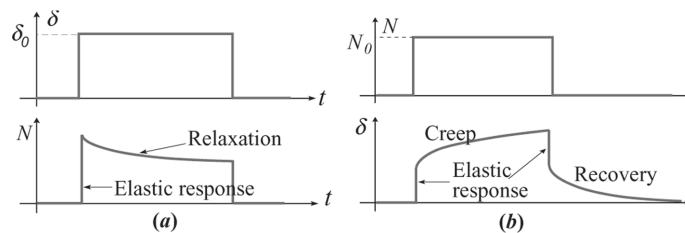


Fig. 2 Behavior of (a) relaxation, and (b) creep at a viscoelastic contact interface

unde-formed configuration. Because creep and relaxation are two aspects of the same viscoelastic phenomena, the two functions are related (Findley, *et al.* 1976, Johnson 1985, Fung 1993).

Fig. 2(a) proposed a model of separation of elastic function from the temporal function (Fung 1993) Thus, in Eq. (1), $N(\delta)$ represents the normal force as a function of the displacement δ as the elastic function. The reduced relaxation function, $g(t)$, representing the temporal function, is a time-decaying function. When normalized to 1 at $t=0$, the function $g(t)$ can be expressed in the following form (Findley, *et al.* 1976, Biagiotti, *et al.* 2005, Tiezzi and Kao 2007, Tiezzi, *et al.* 2005, 2006, Pawluk and Howe 1999, Tiezzi, *et al.* 2007).

$$g(t) = \sum_{i=0}^n c_i e^{-v_i t} = c_0 + c_1 e^{-v_1 t} + c_2 e^{-v_2 t} + \dots \quad (3)$$

with

$$g(0) = \sum_{i=0}^n c_i = c_0 + c_1 + c_2 + \dots = 1 \quad (4)$$

where the parameters c_i and v_i depend on the materials of objects in contact and the exponents $v_i = 1/\tau_i$ identifies the rates of relaxation and creep phenomena with τ_i being the associated time constant.

Furthermore, the contact pressure distribution, $p(r, t)$, at the contact interface is assumed to have a profile of order “ k ” (note: the Hertzian contact (1882) assumes $k = 2$ in Eq. (5))

$$p(r, t) = C_k \frac{N}{\pi a^2} \left[1 - \left(\frac{r}{a} \right)^k \right]^{1/k} \quad (5)$$

where r is the radial coordinate, a is the radius of contact, N is the normal force, and C_k is a constant so that the integration of the pressure distribution $p(r, t)$ over the entire contact area becomes the normal force. The profiles of Eq. (5) as a function of k are illustrated in Fig. 3 for different values of k (Tiezzi and Kao 2007, Tiezzi, *et al.* 2006, Hertz 1882, Xydas and Kao 1999, Kao and Yang 2004), representing stiff elastic to compliant non-linear contacts.

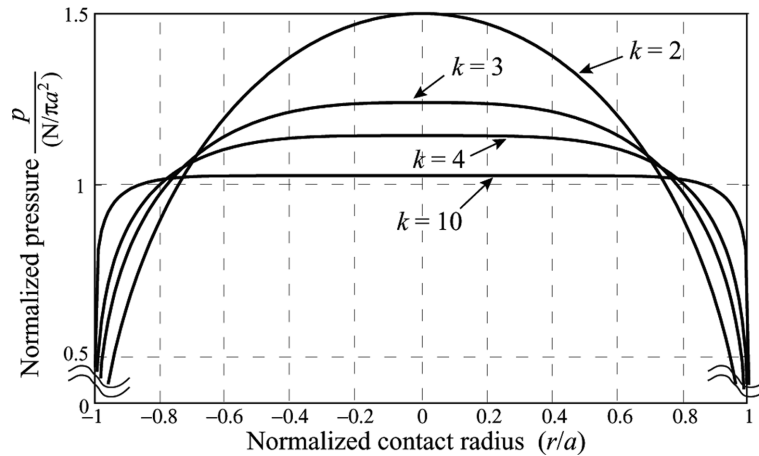


Fig. 3 Typical pressure distribution over a circular contact area at a viscoelastic contact interface

2.2. SACST technology

In this section, we introduce an application of the contact interface with modeling and control which can improve quality of life for the diabetics. The technology, when implemented on footwear, automotive seating, airplane seats, beds, and mattresses can result in technological improvements over the status quo. In Kong, *et al.* (2008), the authors discussed a method for detecting abnormalities in human gait by using smart shoes with fuzzy logic algorithm. The phases of human gait were detected based on four foot pressure sensors. The reference gait also can be used to detect deviation from the reference for diagnosis.

Smart anthropomorphic contact surface technology (SACST) (Diabetes 2007) empowers surfaces at the human contact interface to enhance ergonomic comfort by automatically changing the contact surface and interface. A SACST system consists of a surface that comes in contact with some part of the human body and is controlled by a microprocessor-based system. The contact interface, while responding to the user, can adjust its shape, firmness or temperature to optimize the users comfort level, based on modeling of contact interface and pressure distribution. The change of the contact surface is controlled by either a microprocessor-based or mechanical system.

Through distributed bladders embedded in contact interface with such technology, the active contact surface can render the required shape or be made to accommodate abnormal distributions of contact pressure. As a case in point, diabetic patients often suffer from neuropathy (Day 1995, Diabetes 2007) making them unable to sense foreign objects, such as a pebble, in their shoes. Such foreign object can cause ulcer and, if not detected and treated in time, can result in amputation of the foot (Day 1995). As of 2005, there are over 20 millions diabetics in the US-7% of the population, of which nearly 1/3 were undiagnosed (Day 1995, Diabetes 2007, HCFA 2002). The application of the theory of contact interface and technology can be shown in Fig. 4 in which the pressure distribution for a typical subject is shown. The figures show referential results of pressure measurement at contact interface of feet and the loci of centroids of local contact patches. For local small contact patches, a factor of k in the range of 2-4 in Eq. (5) for biomedical soft contact is not uncommon. The contact areas are 20.50 and 22.98 in²,

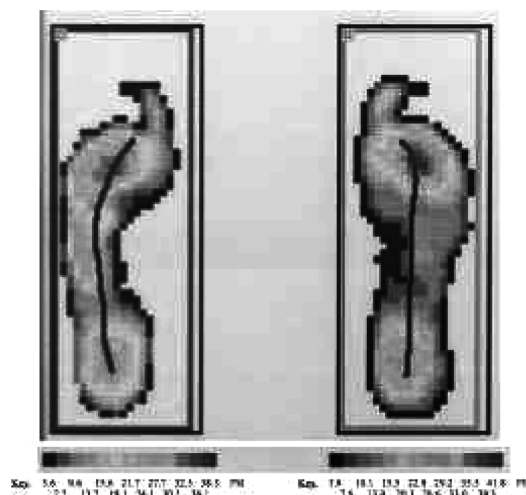


Fig. 4 Pressure distribution at contact interface between feet bottom and shoes, measured using a pressure sensing mat, that can serve as a reference or model for diagnosis

respectively. The figures show that high pressures take place at the ball of the feet with pressure of about 39 psi.

When a foreign object, such as a pebble, is introduced in the shoes, the diabetic patient with neuropathy cannot detect the existence of such object. The pressure sensors, however, will be able to detect the deviation from the model pattern and alert the patient with the high risk of local ulcer due to the pressure point of the pebble. Diabetic patients with neuropathy can wear therapeutic shoes with such technology and model in Eq. (5) in order to reduce incidents of ulcers and to prevent the recurrence of them. This will improve the quality of life for the diabetics. It is noted that the SACST technology described here is different from that in Kong, *et al.* (2008) and yet serving similar purpose for patients needing care.

2.3. FDD using fingerprint analysis in contact interface

Fault detection and diagnosis (FDD) is a technique to make intelligent diagnosis through fingerprint analysis using signal processing tools such as wavelet analysis. Wavelet analysis can decompose signals to *approximate* (cA) and *detailed* (cD) components (see Appendix A). It has an advantage over other signal processing tools in presenting both time-domain and frequency-domain information by decomposing signals with low-pass and high-pass filters. Here, we illustrate the usefulness of wavelet analysis by examining the force signals of the viscoelastic contact as a function of time in Fig. 5 and performing wavelet analysis on the signal. The original signal in the top plot of Fig. 5 is brought to compare with the cD_3 (third-level detailed component) in the plot at the bottom half. The raw data in Fig. 5 show the increase in contact force initially, followed by viscoelastic relaxation period, and finally unload to zero contact force. The corresponding cD_3 components of the wavelet analysis show the fingerprint of valley during the loading stage. When the loading stage changes to the relaxation period, a different fingerprint of cD_3 is seen in which a peak and transition from valley were resulted. This is followed by a gradual decrease along the decay of relaxation in the raw data. Finally, another peak was found at the unloading stage, as shown in the figure.

The transition between segments of viscoelastic contact force plays an important role in recognizing each type of characteristics of fingerprints. Such FDD technique will be very useful for the diagnosis of biomedical tissues, and the processing of sensory information obtained from various sensors and sensor networks. In the next section, we will present a comparison of simulation results of cD_3 using a signal similar to that in Fig. 5.

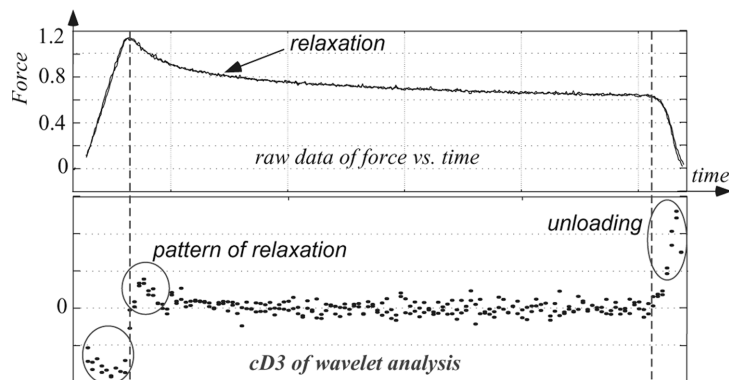


Fig. 5 Application of fingerprint analysis using the wavelet signal decomposition

2.4. Comparison of simulation results of viscoelastic contact with relaxation

The pattern of the contact force in Fig. 5 is adopted in Fig. 6 to perform simulation of fingerprints with different ramp (loading) rate in Fig. 6(a), and with different time constants of relaxation in Fig. 6(b). The results can be employed in the FDD fingerprint analysis to compare different viscoelastic contact interface that involves holding the contact with relaxation of exponentially decaying contact force. As the data in the human grasping experiments in Burstedt, *et al.* (1999) suggest, human beings tend to relax grasp force normal to the contact surface when grasping and holding an object with fingers. The comparison and simulation presented here can shed lights on the analysis of such type of biomedical contact interface.

Next, we define the *time constant* of the exponentially decaying relaxation with $e^{-v_i t}$ as

$$\tau_i = \frac{1}{v_i}$$

With this definition, the amount of decay after one time constant is 63%. Shorter time constant makes faster the exponentially decaying response of relaxation.

From the simulation results in Fig. 6, the following observations are in order for the cD_3 wavelet components based on the raw signals in Fig. 6(a) and (b).

- In general, the ramp (loading) period in the plot of raw signals results in a valley in cD_3 . The subsequent relaxation curve of the raw signals results in a peak above zero in cD_3 followed by decaying cD_3 response. This general response is shown in both Fig. 6(a) and (b).
- Faster ramp rate results in deeper valley in cD_3 response. This is shown in Fig. 6(a) in which the \textcircled{A} curve has a deeper valley than \textcircled{D} , with \textcircled{B} and \textcircled{C} lying in between.
- When the ramp changes to relaxation period with exponential decay, a peak followed by gradual decrease is resulted in cD_3 . This peak occurs at different time depending on the transition from ramp to relaxation of the raw signals, as shown in Fig. 6(a).
- When the relaxation decay is of the same time constant, the shape of rise to peak and the subsequent decay appear to be the same, as shown in the peaks of Fig. 6(a).

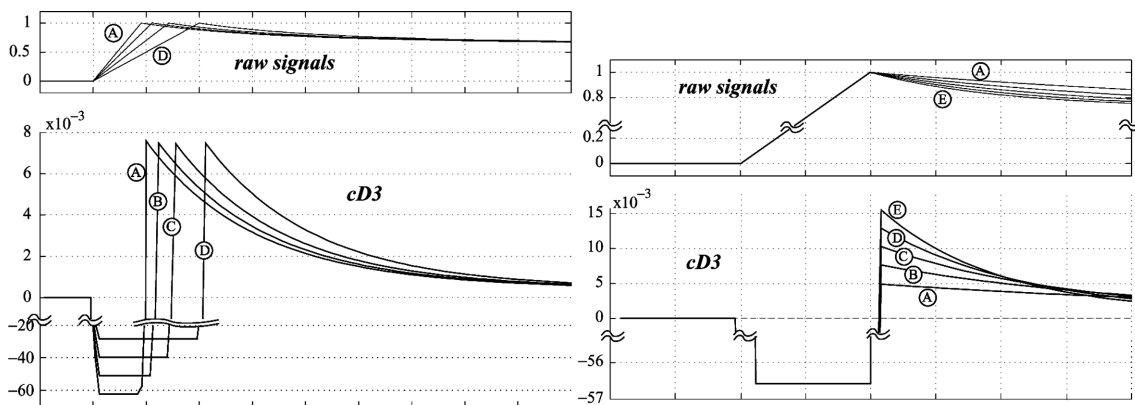


Fig. 6 (a) *Left*: Comparison of cD_3 wavelet component for typical viscoelastic contact at different ramp (loading) rates but with the same decaying relaxation function. (b) *Right*: Comparison of cD_3 wavelet component for typical viscoelastic contact at several decaying relaxation functions with different time constants, at the same ramp (loading) rate

- If the relaxation decay is faster (i.e. with a smaller time constant), higher peak is observed. This is shown in Fig. 6(b) in which \textcircled{A} has the longest time constant and slowest decay, resulting in the lowest peak. On the other hand, \textcircled{E} has the shortest time constant (decays the fastest), resulting in the highest peak.

Here the fingerprint analysis is performed using the cD_3 component, although cD_1 and cD_2 can also be employed with different levels of details.

3. Signal-based approach for FDD

Pneumatic systems are often found in manufacturing floors for automation and in robotic systems such as end-effectors or pneumatic servo for control. The supervision of systems is important in modern manufacturing automation in order to improve maintainability and availability, as well as to protect environment and personnel. The purpose of fault detection and diagnosis (FDD) is to detect faults of systems (such as leakage or blockage) and to diagnose the size and location of the faults early for counter-measures. See Table 1 for a comparison in detection and diagnosis using FDD. A good FDD system can prevent shutdown of system due to the failure of individual devices that often leads to loss of production time and profits. The study of FDD analysis for mechanical and pneumatic systems, as discussed here, ultimately will directly or indirectly improve our quality of life. In the following sections, experiments are conducted and the data are applied in the FDD analysis for diagnosis.

3.1. Literature and research in signal-based FDD

During the last few years, many research results have been presented in the field of process supervision and fault diagnosis. Due to the large variety of process characteristics, many different approaches for the fault detection and diagnosis (FDD) have been introduced. The task of fault detection is to detect the existence of faults, depending on the presence or absence of an appropriated process model; whereas, the task of fault diagnosis consists of the detection of the type, size, and location of the faults as well as their time of detection. There are three main methods of fault diagnosis: (1) human expertise, (2) pattern recognition, and (3) knowledge-based systems (Isermann 1997, Kao, *et al.* 2003). The development of process fault detection method based on modeling, parameter and state estimation was summarized by Isermann (1997). Simani, *et al.* reviewed the history and discussed the methods used in this field in their book (2003). Various techniques including fuzzy logic, neural networks, ... etc., have been proposed, such as those in Chang, *et al.* (2002), Skoundrianos and Tzafestas (2002).

3.2. Experimental setup for FDD analysis

A sensor-integrated, real-time control and data acquisition system was constructed to operate a mechanical-pneumatic system designed to study sensor-based fault detection and diagnosis (FDD). The

Table 1 A comparison and analogy of fault detection and diagnosis versus medical diagnosis

	<i>analogy in medical field</i>	<i>leakage in pneumatic systems</i>
detection	a symptom exists	a leakage exists
diagnosis	determination of the root cause of the symptom and how serious it is	determination of the size and location of the leakage

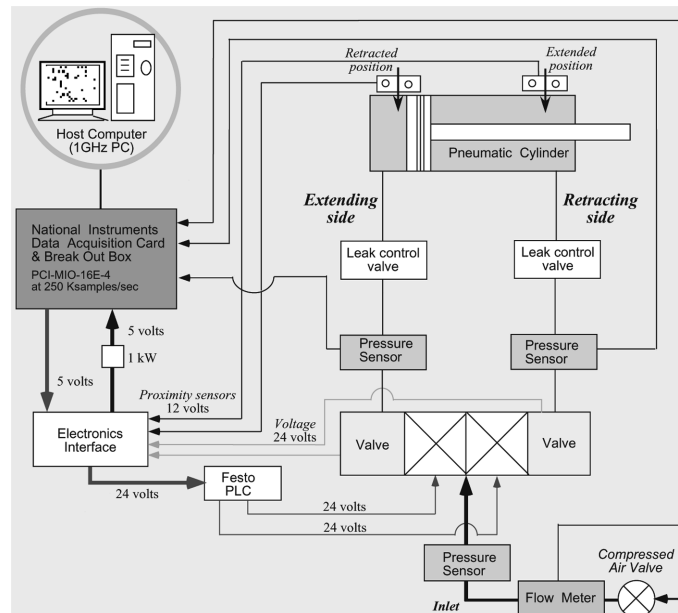


Fig. 7 Schematic of the pneumatic system for experiments

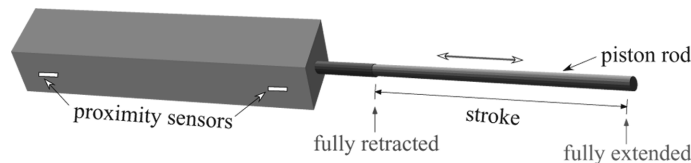


Fig. 8 Piston position and terminology of the pneumatic cylinder

mechatronic system consists of hardware, software, and interface. The integration of sensors and actuators into the mechanical system is shown in Fig. 7. During the regular operation, the piston of the pneumatic cylinder, controlled by two solenoids of the control valve, moves back and forth between the extreme right (extended) and left (retracted) positions, as shown in Fig. 8. Two proximity sensors are employed to detect the extend or retract position. A complete run cycle is defined as a full cycle which includes an extend stroke and a retract stroke, as shown in Fig. 9. Pressure sensors are located at different places of the transducer-integrated system. Bulk flow meters, including volumetric and mass types, were employed to measure flow rates at various locations. In the integrated system, all sensors and actuators are installed and can be enabled and accessed from the PC directly for data acquisition and control. The PC host computer is configured for both real-time control and post-process data analysis. A graphic user interface (GUI), written in Visual C++, performs real-time data acquisition and process monitoring via the NI PCI-MIO-16E-4 DAQ, and stores data periodically for post-process analysis using MATLAB (Li and Kao 2004, Kao, *et al.* 2003). In the current configuration, the pneumatic cylinder is controlled to move back and forth between the two extreme positions under a range of sampling rate at 100-15000 Hz. Each complete cycle of the extending and retracting strokes takes about two seconds plus delays between strokes. The sampled signals are saved for post-process analysis.

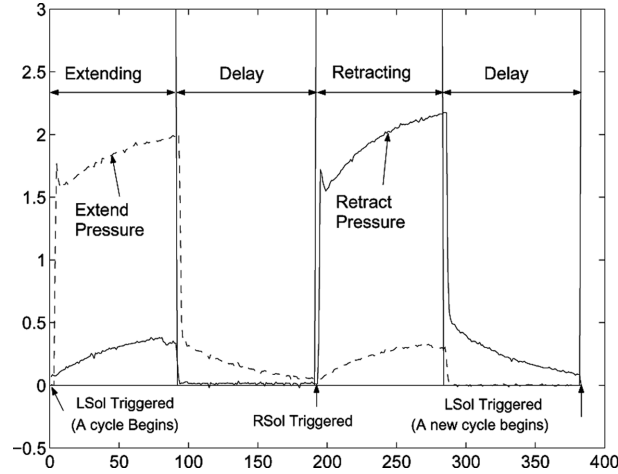


Fig. 9 A typical cycle of pressure signals obtained in experiments, used as a reference in wavelet-based FDD

3.3. Signal-based FDD using wavelet transform

Fig. 9 shows a complete cycle of operation with four segments: extending stroke, retracting stroke, and delays between the two working strokes for reversing of directions. Three-level wavelet decomposition is applied here on each segment of the three signals as formulated in Eqs. (15) and (16). After decomposition and reconstruction, the original data are separated into components with different frequencies.

Many choices of features can be extracted, including the coefficients themselves or any combination of coefficients. In this paper, we adopt a non-exhaustive and suboptimal search (Theodoridis and Koutroumbas 2003). Statistical properties of the original signals and their wavelet coefficient are candidates for features. The maximum, averages, variances, moments of the feature candidates are evaluated, and the most significant ones are chosen. Then, features from each segment are combined to form a *feature vector*. Next, we repeat such procedures for all the data obtained from different locations and sizes of leakage to create the relationship between the feature vectors and different levels of leakage. The relationship can be divided into three groups, each corresponding to different configuration of leakage. Three classes are created: *extending leakage class*, *retracting leakage class*, and *leakage at both sides class*.

3.3.1. Classification of leakage configuration

Based on the individual features selected, the fingerprint of the characteristics of signals can be captured by the wavelet method, with DB2 coefficient. Two of such coefficients of wavelet transform¹ of the raw signals of flow rate measurements are shown in Figs. 10 and 11. Each “cluster” of points in the plots represent data from 80 cycles of operations.

In Fig. 10, the leakage in the retracting side was clearly shown to be under that in the extending side in the cA_3 plot. This plot resembles the time-domain information. In the cD_1 plot in Fig. 10, the information resembles frequency-domain characteristics which clearly depicts the different clusters of data in the extending and retracting sides. The clusters (in circles) of data in this plot are corresponding to the falling edge of the signals obtained by sensors. By combining the information of both plots in

¹Here, we employ cA_3 and cD_1 owing to the specific nature of the pneumatic system at hand and the effectiveness of the data analysis

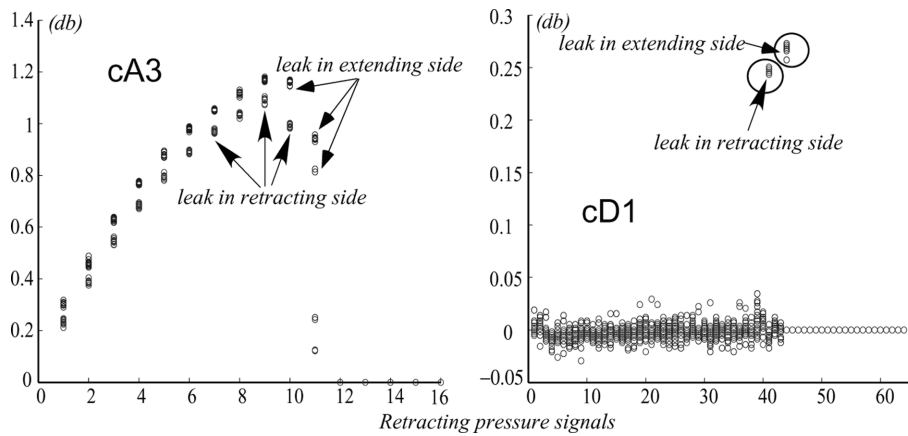


Fig. 10 Diagnosis of leakage location using the approximate coefficients, cA_3 , and the detail coefficient, cD_1 with clearly distinguishable clusters of data for diagnosis. The DB2 wavelet was used

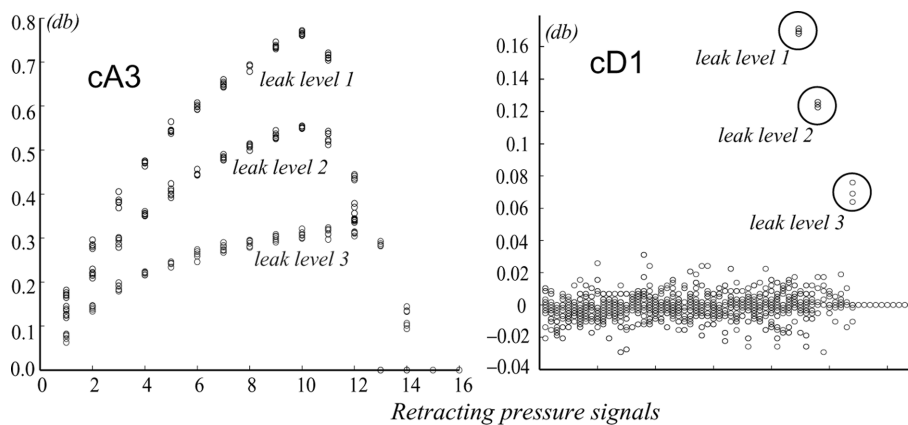


Fig. 11 Diagnosis of size of leakage using both cA_3 and cD_1 with three clusters of data for diagnosis

Fig. 10, diagnosis on the leaking location, whether it is at the extending or retracting, can be made.

In Fig. 11, the characteristics of different levels of leakage are plotted and compared. Again, in the cA_3 plot, different levels of leakage in the retracting side are used for the purpose of diagnosis. Any unknown fault with different levels of leakage in the retracting side can be identified when compared with the plot. In the cD_1 plot, the clusters indicate the frequency-domain information of different leakage levels. The three circled clusters represent not only the level of leaks (vertical direction) for diagnosis, but also the elongation in time (horizontal direction) to complete a stroke, indicating that the time it takes to complete the cycle is gradually elongated from leak level 1 to 3. Such different fingerprints is very useful in diagnosis. Figures similar to Fig. 11 (which is for the retracting side only) can be constructed for the extending side as well.

3.4. Vectorized map for analytical FDD

In this section, we present an innovative methodology for analytical FDD. When two sets of signals of similar nature are obtained, a calibrated vectorized map can be obtained, just like the 2D Cartesian

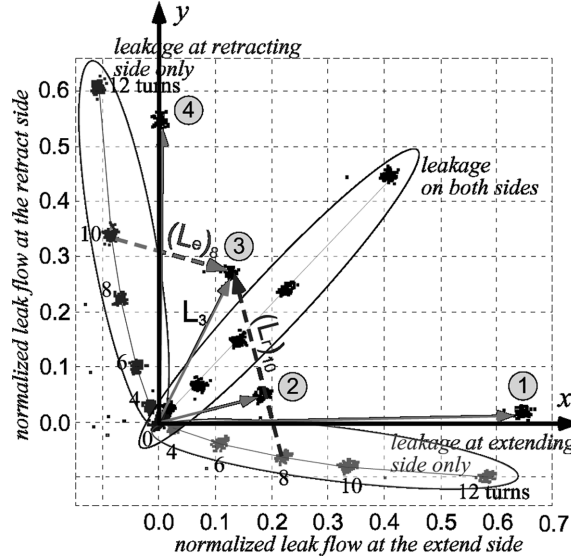


Fig. 12 Analytical vectorized map for diagnosis of leakage

plane in which a coordinate (x, y) represents a vector of $x\vec{i} + y\vec{j}$ with \vec{i} and \vec{j} being the bases (or unit vectors) in the x and y axes. Likewise, the quantity of two faults can be calibrated to form a pair of basis for a vectorized map. For example, we can assign the two axes as the amount of leak flow in the extending and retracting directions, respectively. When the two axes are calibrated, they form a 2D map with any vector on the map representing corresponding combination of leak flows in both directions. In the following, we will use an example with experimental results to explain this methodology.

The total flow integrated for the signal obtain by the flow meter (flow rate) can be employed to render such a 2D plot to quantitatively determine the location and size of leakage, as shown in Fig. 12. In this figure, both axes are calibrated and scaled with respect to the standard flow at no leakage in respective axis. We observe that the data over 100 cycles tend to cluster, though occasional scatter exists. In addition, the leakage calibration in either side (horizontal and vertical clusters enclosed by ellipses) was symmetric with respect to the near 45° clusters of data that represent equal amount of leakage on both extending and retracting sides. The leakage is in the increasing order of 4, 6, 8, 10 and 12 turns of the leak control valve knob, as indicated in Fig. 12.

Based on the three elliptical clusters of known sensor data, the four unknown data clusters encircled with numbers ①②③ and ④ can be readily diagnosed. For example, circle ③ can be found to have 8 turns of extend leak and 10 turns of retract leak. As indicated in Fig. 12, the vector drawn to the cluster ③ is the vector sum of corresponding leakage along the respective axis. Other clusters also follow the same 2D vector operation. In a vector modeling equation, we can write

$$\vec{L}_3 = (\vec{L}_e)_8 + (\vec{L}_r)_{10} \text{ or } \vec{L} = \vec{L}_1 + \vec{L}_2 \quad (6)$$

where \vec{L}_e and \vec{L}_r are leakages of the extending and retracting sides, respectively, with subscripts in numbers representing number of turns, and \vec{L}_3 is the leakage measured at ③. Based on Eq. (6), the vectorized map in Fig. 12 can be visualized as having two bases with coordinates. Any point on the map (a particular fault configuration) is simply a linear combination of constants (coordinates) times

the unit vectors along the two bases. Furthermore, the two bases in Fig. 12 can be transformed easily to form two orthogonal bases², as will be discussed in Section 3.4.1, by an affine transformation, which will be discussed in the next section.

The vectorized pattern map is a very effective technique for FDD because both the location and size of leakage can be represented by the vector space map using selected sensor data. This technique also can be extended to a system of N bases by constructing sensor data of N -manifold as indicated in Eq. (7), similar to the concept of the 2D case demonstrated in Eq. (6).

$$\text{in } N\text{-manifold: } \vec{L} = \vec{L}_1 + \vec{L}_2 + \dots + \vec{L}_n \quad (7)$$

The interpretation of sensor data again will render the FDD of size and location of leak. The N -manifold vectorized map of leakage can be implemented in a stepwise method. Namely, The selected features are ordered according to their abilities in distinguishing differences between leakage configurations. To start the diagnosis, only two features with the 2D map, as discussed earlier, are used. If the vector made up of the two features succeeds in FDD, a successful diagnosis is made and the process will stop. If there is still ambiguity, other pairs of features can be added one by one to the space until it succeeds in FDD. It is important to note that even after a successful diagnosis is made with one 2D vectorized map, other pairs can be employed to confirm the diagnostic results. Such *redundancy* can enhance the confidence of the FDD results.

3.4.1 Affine transform for vectorized maps

In order to map the points and reference coordinates in Fig. 12 to within the first quadrant of the orthogonal bases with (u, v) coordinates in Fig. 13, we define the generic affine transform (without translation) as follows:

$$\begin{bmatrix} u \\ v \end{bmatrix} = \begin{bmatrix} a_{11} & a_{12} \\ a_{21} & a_{22} \end{bmatrix} \begin{bmatrix} x \\ y \end{bmatrix} \quad (8)$$

where x, y are the coordinates obtained using the raw experimental data, as shown in Fig. 12, and u, v are the coordinates after the affine mapping, as shown in Fig. 13. It is the nature of the affine transform in Eq. (8) that linear and angular dilation will take place. In the following, we will define both dilations for the purpose of calibration of experimental data for diagnosis.

The distance between a given point and the origin of the coordinates in Fig. 12 is

$$l_{xy}^2 = x^2 + y^2 \quad (9)$$

After the affine transformation, the distance in the (u, v) coordinates becomes

$$\begin{aligned} l_{uv}^2 &= u^2 + v^2 = (a_{11}x + a_{12}y)^2 + (a_{21}x + a_{22}y)^2 \\ &= (a_{11}^2 + a_{21}^2)x^2 + (a_{12}^2 + a_{22}^2)y^2 + 2a_{11}a_{12}xy + 2a_{21}a_{22}xy \end{aligned} \quad (10)$$

²Although we are more accustomed to orthogonal bases, such as those represented in the Cartesian coordinate frame, the orthogonalization is not necessary theoretically, as long as the bases are independent of each other. For the sake of convenience, however, orthogonalization will be discussed in Section 3.4.1.

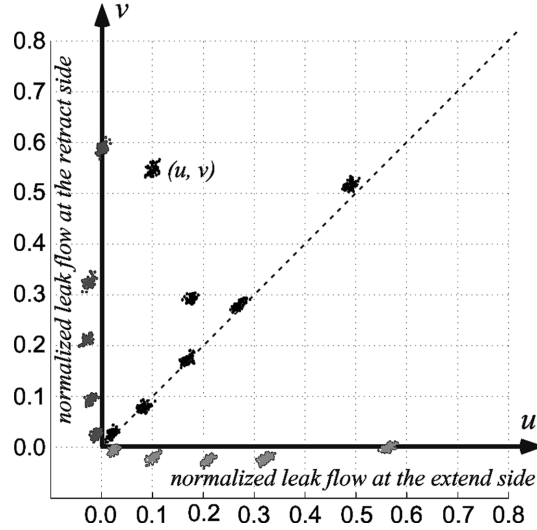


Fig. 13 The analytical vectorized map after the affine transformation

Therefore, the *linear dilation* of the affine transformation can be characterized by the following ratio

$$r = \frac{l_{uv}}{l_{xy}} \quad (11)$$

The linear dilation r in Eq. (11) can be obtained from Eqs. (9) and (10). In addition, both the cross product and dot product can be used to calculate the angle between the vectors from the origin to the given point before and after the affine transform. Here, the dot product is utilized to obtain

$$\cos \theta = \frac{\vec{v}_1 \cdot \vec{v}_2}{|\vec{v}_1| |\vec{v}_2|} \quad (12)$$

In the case, we have $\vec{v}_1 = x\vec{i} + y\vec{j}$, $\vec{v}_2 = u\vec{i} + v\vec{j}$, where \vec{i} and \vec{j} are unit vectors along the horizontal (x) and vertical (y) directions of the orthogonal coordinate system in Fig. 12, respectively. Inserting the values of x , y , and u , v into the above equation, we obtain

$$\begin{aligned} \cos \theta &= \frac{xu + yv}{\sqrt{x^2 + y^2} \sqrt{u^2 + v^2}} = \frac{a_{11}x^2 + (a_{12} + a_{21})xy + a_{22}y^2}{l_{xy}l_{uv}} \\ &= \frac{1}{r} + \frac{(a_{12} + a_{21})}{r} \frac{xy}{x^2 + y^2} \end{aligned} \quad (13)$$

where l_{xy} and l_{uv} are defined in Eqs. (9) and (10), respectively. The quantity $\cos \theta$ defined in Eq. (12), and expressed in Eq. (13), can be used to calculate the *angular dilation* of the affine map.

3.4.2. Affine transform for the case at hand

In the example presented in Figs. 12 and 13, the affine transform as defined in Eq. (8) can be determined as

$$A = \begin{bmatrix} 1 & 0.18 \\ 0.17 & 1 \end{bmatrix} \tag{14}$$

based on the experimental data and calibration in order to make the non-orthogonal axes in Fig. 12 into the orthogonal axes in Fig. 13. For the point $(x, y)=(0.15, 0.15)$ in Fig. 12, for example, the coordinates after the affine map are $(u, v)=(0.177, 0.1755)$. The linear dilation is found to be $r = 1.175$, based on equations defined above. The angular dilation is calculated as $\cos\theta = 0.99999$ with corresponding angle of nearly 0° . Note that this point is along the 45° line since $x=y$; thus, the angular dilation is nearly zero. The mapped coordinates $u \neq v$ because the affine transform matrix A is not symmetric.

Take another point for an example with $(x, y)=(0.5, 0.2)$. Follow the same procedure, we obtain $(u, v)=(0.536, 0.285)$, with linear dilation of $r = 1.1273$ and angular dilation of $\theta=6.2^\circ$. In this case, the point has been stretched outward (away from the origin) and angularly shifted for 6.2° in the counterclockwise direction after affine map. Some results are summarized in the following table.

(x, y)	(u, v)	r	θ
(0.15, 0.15)	(0.177, 0.1755)	1.175	0.2°
(0.5, 0.2)	(0.536, 0.285)	1.1273	6.2°
(0.1, 0.35)	(0.163, 0.367)	1.1032	8.0°

These parameters can be used for the purpose of diagnosis using the 2D affine map once an unknown data is identified on the map. The leak flows on the extending and retracting sides are treated as the coordinates, and the vector diagnosis as introduced in this section can be employed directly for diagnosis, using the affine map. The advantage of the affine map is the establishment of geometric data in the orthogonal coordinates (u, v) to afford easy and straightforward diagnosis.

3.4.3. Using the Voronoi diagram for diagnosis

An alternative to the vectorized map methodology for diagnosis is the Voronoi diagram. The Voronoi diagram of a collection of geometry objects is a partition of space into cells, each of which consists of the points closer to one particular object than to any other. A 2D Voronoi diagram is used to create class boundaries between features as in Fig. 14 for the 2D pattern map in Fig. 12. Voronoi diagram is a fast way for k -Nearest Neighbor Rule, which is defined to assign unknown pattern to the majority class among k nearest neighbor using a performance optimized value for k (Jain, *et al.* 2000). The advantage of this method is the easy implementation of algorithm computationally.

In the following, the 2D vectorized map obtained in Fig. 12 is used to illustrate how the technique of Voronoi diagram can be used. First, the centroids of all the clusters are found. Next, a perpendicular bisecting line to the line segment joining two neighboring centroid are drawn. These perpendicular bisecting lines interest to connect and form different regions shown in Fig. 14.

Each closed region of geometry can be used for diagnosis. If an unknown data point falls within a region, it can be classified as similar to the reference cluster in that same region. When an unknown data point is at the boundary of these regions, additional criteria can be applied to make the diagnosis.

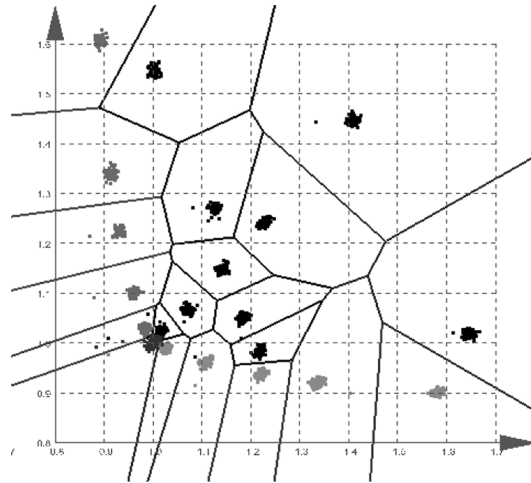


Fig. 14 The class boundaries between feature vectors with Voronoi diagram

3.5. Discussions

In the preceding section, signal-based FDD using wavelet and vectorized map are introduced. Successful diagnosis of manufacturing systems to prevent failure often contributes to the improvement of quality of life with better product quality and economic betterment.

The approximate (cA_3) and detail (cD_1) coefficients are used to classify leakage location in Fig. 10, in which we find leakage at two different locations showing distinct features in quasi-time and quasi-frequency domains. Application of these two coefficients enables us to perform the intelligent diagnosis of faults in leakage and its location. Fig. 11 is used to diagnose levels of leakage. It can be seen that the results of cA_3 show the order of magnitude of reduction in pressure and the elongation of time lag when the level of leakage is increased. Furthermore, the cD_1 coefficient reflects the falling edge of pressure change when the stroke of travel changes which results in clear indication of clusters of data that can be used for diagnosis of both quantity of leak and the time lag due to leak.

The vectorized maps not only is intuitive but also is effective for the applications in diagnosis. When multiple pairs of data can be collected and employed in analysis, it provides *redundancy* in diagnosis which enhances the confidence of the outcomes of FDD. Affine transform with linear and rotational dilations are discussed when such vectorized maps are orthogonalized.

The method using Voronoi diagram is introduced to perform diagnosis. An important advantage of this methodology is that the algorithm lends itself very easily to computational implementation.

4. Conclusions

In this paper, we present the methodology of both model-based and signal-based fault detection and diagnosis (FDD), with the implication of improvement towards a better quality of life. The theory and practice are presented with examples of biomedical contact interface and manufacturing equipment. Using the modeling of contact interface, one can make effective diagnosis of abnormal contact patterns which in turn can help diabetic patients to detect and treat the cause of such abnormal contact before

ulceration sets in. Fingerprint analysis on typical contact and relaxation behavior commonly found in biomedical and/or soft tissues are presented and discussed.

The signal-based approach with wavelet method is employed to extract features from the sensor signals, such as pressure, flow rate, or flow, to implement intelligent FDD. The methodology was demonstrated to be capable of determining the size and location of the leakage fault by employing the wavelet transform with approximate and detailed components (cA and cD). Various methodology including analytical vectorized map, affine transformation, and Voronoi map are presented for analytical FDD. The vectorized map with affine transform and redundancy can enhance the confidence of diagnosis, especially in the presence of ambiguity in data analysis. Such FDD techniques can be applied in manufacturing automation to increase the productivity by reducing unnecessary shutdown of systems due to faults undetected in time.

Acknowledgment

This work has been supported by National Science Foundation (NSF) Grants CMS0428403. This work is also supported by a US-Japan (NSF-JST) joint research grant with Professor Makoto Kaneko at Osaka University (NSF-CMMI0800241; Program Director: Dr. Shih Chi Liu). The authors also thank Craig Capria's assistance and comments.

References

- Biagiotti, L., Tiezzi, P., Melchiorri, C. and Vassura, G. (2005), "Modelling and identification of soft pads for robotic hands", *Proc. IEEE Int. Conf. on Intelligent Robots and Systems, IROS*, Edmonton, Canada.
- Burstedt, M. K., Flanagan, J. R. and Johansson, R. S. (1999), "Control of grasp stability in humans under different frictional conditions during multidigit manipulation", *The J. Neurophysiology*, **82**(5), 2393-2405.
- Chang, S., Lin, C. and Chang, C. (2002), "A fuzzy diagnosis approach using dynamic fault trees", *Chemical Eng. Sci.*, **57**, 2971-2985.
- Chui, C.K. (1992), *An Introduction to Wavelets*, Academic Press.
- Daubechies, I. (1992), *Ten Lectures on Wavelets*, Society for Industrial and Applied Mathematics.
- Diabetes Day-by-Day, (1995), "Neuropathy and foot care", American Diabetes Association, Tech. Rep.
- National Diabetes Information Clearinghouse (NDIC) (2007), "<http://diabetes.niddk.nih.gov/dm/pubs/statistics/>", National Institute of Diabetes and Digestive and Kidney Diseases (NIDDK), Tech. Rep. 2007.
- Findley, W.N., Lai, J.S. and Onaran, K. (1976), *Creep and Relaxation of Nonlinear Viscoelastic Materials*. North-Holland Publishing Company.
- Fung, Y. C. (1993), *Biomechanics: Mechanical Properties of Living Tissues*, Springer-Verlag.
- Hertz, H. (1882), *On the Contact of Rigid Elastic Solids and on Hardness, chapter 6: Assorted Papers by H. Hertz*. MacMillan, New York, November.
- Isermann, R. (1997), "Supervision, fault-detection and fault-diagnosis methods -an introduction", *Control Eng. Practice*, **5**(5), 639-652.
- Jain, A.K., Duin, R.P.W. and Mao, J. (2000), "Statistical pattern recognition: A review", *IEEE Trans. on Pattern Analysis and Machine Intelligence*, **22**(1), 4-37.
- Jakubek, S. and Jörgl, (2000), "Fault-diagnosis and fault-compensation for nonlinear systems", *Proceedings of the American Control Conference*, June, pp. 3198-3202.
- Jensen, A. and la Cour-harbo, A. (2001), *Ripples in Mathematics: The Discrete Wavelet Transform*, Springer.
- Jin, J. and Shi, J. (2001), "Automatic feature extraction of waveform signal for in-process performance improvement", *J. Intell. Manufacturing*, **12**, 257-268.
- Johnson, K. L. (1985), *Contact Mechanics*, Cambridge University Press.

- Kao, I. and Yang, F. (2004), "Stiffness and contact mechanics for soft fingers in grasping and manipulation", *the IEEE Trans. of Robotics and Automation*, **20**(1), 132-135.
- Kao, I. and Zhang, K. (2007), "Miniaturized sensors for intelligent system fault detection and diagnosis", *Proceedings of the SPIE SSN 07 Conference, SSN07*. San Diego, California: SPIE, March 18-22.
- Kao, I., Kumar, A. and Binder, J. (2007), "Smart MEMS flow sensor: theoretical analysis and experimental characterization", *IEEE Sensors J.*, **7**(5), 713-722.
- Kao, I., Kumar, A., Boehm, C. and Binder, J. (2006), "Intelligent diagnosis of mechanical-pneumatic systems using miniaturized sensors", *Proceedings of the SPIE Smart Structures and Materials/NDE Meeting*, vol. 6174. San Diego: SPIE, Feb-Mar, pp. 617 422-1-617 422-12.
- Kao, I., Li, X. and Binder, J. (2003), "Fault detection and diagnosis of pneumatic systems", *NFPA's Educator/Industry Summit*, Indianapolis, Indiana, October.
- Kao, I., Lynch, K. and Burdick, J. (2008), *International Robotics Handbook: Contact Modeling and Manipulation*. Springer-Verlag, vol. IV, ch. 27.
- Kong, K., Bae, J. and Tomizuka, M. (2008), "Detection of abnormalities in a human gait using smart shoes", *Proc. of SPIE*, **6932**(69322G).
- Li, X. and Kao, I. (2004), "Fault detection and diagnosis for pneumatic system using wavelet transform and feature extraction", *SCI-2004, the 8th World Multi-Conference on Systemics, Cybernetics, and Informatics*, Orlando, Florida, July 18-21, pp. 320-325.
- Li, X. and Kao, I. (2005), "Analytical fault detection and diagnosis (FDD) for pneumatic systems in robotics and manufacturing automation", *IEEE/RSJ International Conference in Intelligent Robots and Systems, IROS 2005*, Alberta, Canada, August 2-6, pp. 2517-2522.
- Pawluk, D.T.V. and Howe, R.D. (1999), "Dynamic lumped element response of the human fingerpad", *ASME J. Biomech. Eng.*, **121**(2), 178-183.
- Pittner, S. and Kamarthi, S. V. (1999), "Feature extraction from wavelet coefficients for pattern recognition task", *IEEE Transactions on Pattern Analysis and Machine Intelligence*, **21**(1), January.
- Simani, S., Fantuzzi, C. and Patton, R. J. (2003), *Model-based Fault Diagnosis in Dynamic System Using Identification Techniques*, Springer.
- Skoundrianos, E.N. and Tzafestas, S.G. (2002), "Fault diagnosis via local neural networks", *Mathematics and Computers in Simulation*, **60**, 169-180.
- Theodoridis, S. and Koutroumbas, K. (2003), *Pattern Recognition*. Academic Press.
- Tiezzi, P. and Kao, I. (2007), "Modeling of viscoelastic contacts and evolution of limit surface for robotic contact interface", *IEEE Transaction on Robotics*, **23**(2), 206-217.
- Tiezzi, P., Kao, I. and Vassura, G. (2006), "Effect of layer compliance on frictional behavior of soft robotic fingers", *Proc. IEEE Int. Conf. on Intelligent Robots and Systems (IROS 2006)*, Beijing, China, October, pp. 4012-4017.
- Tiezzi, P., Kao, I. and Vassura, G. (2007), "Effect of layer compliance on frictional behavior of soft robotic fingers", *Advanced Robotics*, **21**(14), 1653-1670.
- Tiezzi, P., Vassura, G., Biagiotti, L. and Melchiorri, C. (2005), "Nonlinear modeling and experimental identification of hemispherical soft pads for robotic manipulators", *Proc. of IDETC/CIE ASME Int. Design Engineering Technical Conf. & Computers and Information in Engineering Conf.*, Long Beach, CA.
- U. S. H. C. F. A. (HCFA), "The therapeutic shoe bill: Medicare carriers manual-section 2134", HCFA, Tech. Rep., August 2002.
- Xydas, N. and Kao, I. (1999), "Modeling of contact mechanics and friction limit surface for soft fingers in robotics, with experimental results", *Int. J. Robotic Res.*, **18**(8), 941-950.

Appendix A: Discrete wavelet transform

In this paper, we employ the wavelet transform as a tool for analytical FDD. Many research literatures exist and present results in various fields of study. Some important literature and research studies are listed in the reference (for example: Daubechies, Chui 1992, Jensen and la Cour-harbo 2001), among others). The wavelet transform cuts up data or function and separates them into different frequency and time components for the purpose of studying each components with a resolution matched to its scale. Two procedures can be employed with the decomposition:

1. *Analysis*: start with the coefficients $cA_0(k)$ at scale index j and produce the two sets of coefficients $cA_1(k)$ and $cD_1(k)$ at scale index $j-1$.
2. *Synthesis*: start with the two sets of coefficients $cA_1(k)$ and $cD_1(k)$ at scale index $j-1$ and produce the coefficients $cA_0(k)$ at scale index j

Next, we can show that the two operations of analysis and synthesis are produced by certain filter banks

$$cA_1(k) = \sum_n h_0(n-2k)cA_0(n) \tag{15}$$

$$cD_1(k) = \sum_n h_1(n-2k)cA_0(n) \tag{16}$$

$$cA_0(n) = \sum_k cA_1(k)h_0(n-2k) + \sum_k cD_1(k)h_1(n-2k) \tag{17}$$

Following the filtering, the signal is decimated by a factor of 2, shown in Fig. 15(a). The outputs of the low-pass branch in Eq. (15) are called *approximation coefficients (cA)*. The outputs of the high-pass branch in Eq. (16) are called *detail coefficients (cD)*. This filtering process followed by decimation is referred to as *single-step wavelet decomposition*. The single-step wavelet decomposition can be performed iteratively. At each iteration step, the approximation coefficients from the previous step will be used as the input of the filter bank. As the decomposition process iterates, with successive approximations decomposed in turn, one signal is broken down into many lower resolution components. The processes of one-step and multi-step wavelet decomposition are shown in Fig. 15(b). Conversely, the signals can be perfectly reconstructed from the wavelet approximation coefficients and detail coefficients using the inverse fast wavelet transform (IFWT). The basic idea behind the fast wavelet transform (FWT) algorithm is to represent the mother wavelet as a set of high-pass and low-pass filters in a filter bank, through which the signal is passed. Refer to Daubechies (1992) for more information on the inverse wavelet transform.

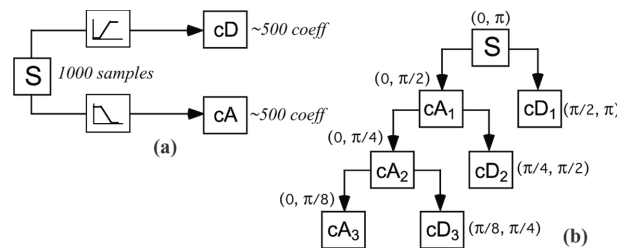


Fig. 15 Two channel decomposition and decomposition tree: (a) two channel decomposition, and (b) decomposition tree